Results in Physics 53 (2023) 107016

Contents lists available at ScienceDirect

Results in Physics

journal homepage: www.elsevier.com/locate/rinp

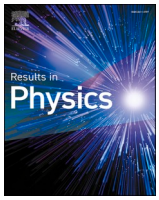

Hydrocarbons (C8–C12) separation in porous metallocavitand M-PPX (M = Cu, Ag, Au): From computational insight

Biswajit Mohanty [a,*], Gopal Avashthi [b,*]

[a] Department of Chemistry, Central University of Haryana, Mahendergarh 123031, Haryana, India
[b] School of Sciences, P P Savani University, NH-8, GETCO, Gujarat-394125, India

A B S T R A C T

High throughput computational approach has been employed to investigate the adsorption and separation of C8–C12 hydrocarbons (HCs) on a tube-shaped metallocavitand, pillarplex (PPX). The Cu (I), Ag (I), and Au (I) seamed PPX and their HC complexes has been examined using density functional theory (DFT), proclaiming Cu-PPX has a higher binding affinity with the HCs whereas Ag-PPX is lower. The thermodynamic properties reveal the host–guest complex is stable at ambient condition. Noncovalent interaction (NCI) analysis shows the interaction of guests within the cavity of PPX is mainly attributed by Van der Waals type. The energy decomposition analysis (EDA) enunciates the percentage contribution of dispersion interaction (ΔE_{disp}) is 59–62%, the electrostatic (ΔE_{elct}) and orbital (ΔE_{orb}) terms have a moderate contribution towards the total binding energy. The Grand canonical Monte Carlo (GCMC) simulation manifests the Cu-PPX and Au-PPX are the ideal hosts with the optimum capacity to store HCs at ambient conditions. The octane uptake is 18.01, 17.50, and 25.31 cm^3STP/g in Cu, Ag and Au-PPX and the uptake reduces upon increasing the HC chain length. The isosteric heat of adsorption (Q_{st}) is corroborated with the computed DFT data at ambient setup. The ideal adsorption solution theory (IAST) claims the C8 selectivity in Cu, Ag and Au-PPX is optimum at 298 K and the increasing temperature from 298 K to 323 K, the selectivity of the C9 and C12 in Cu-PPX and Au-PPX, respectively is remarkable after the complete separation of C8. Hence Cu-PPX and Au-PPX is the potential candidate for industrial use to separate the heavy HCs.

Introduction

Hydrocarbon (HC) mixtures are separated into various components owing to their importance in the production of fuels and basic feedstocks for chemical industries [1]. The harmony of their physicochemical property and reactivity is a major stumbling block for the separation of HCs from their corresponding mixtures [2–4]. The conventional method of separation, integrated by the use of membranes, cryogenic distillation, and adsorption (physical and chemical) emerged as a potential method for separation but are exorbitant [5–8]. Liquid phase/gas phase adsorption is the most usual way to separate lower HCs from their corresponding higher HCs due to its ease of operation and low energy consumption [9]. A tenacious material is required for liquid/gas phase adsorption; hence several attempts have been put forth to find a promising material with optimum efficiency for the adsorption and separation of higher HCs [10].

The nanoporous molecular sieves such as metal–organic framework (MOF), zeolites, and activated carbons, and mechanically interlinked molecules are peerless materials that attracted notable attention because of their fascinating structures, facile synthesis, and manifold applications [11–17]. MOFs are ideal adsorbents for gas adsorption behavior due to the large surface areas, tunable surface functionalities, and high adsorption affinities [18,19]. Similarly, zeolites and activated carbons are abundant and inexpensive molecular sieves and have been used in the various adsorption process [20]. The foregoing study claims that hydrophobic MOFs, such as zeolitic imidazolate framework-8 (ZIF-8) and metal-azolate framework-6 (MAF-6) are hybrid MOFs for the separation of n-alkanes (up to C10) by using gas chromatography [21–24]. Jhung et al observed that the MAF-6 and Cu-BTC showed the selectivity for the adsorption of C12 and C7 respectively from the C8 [24]. Ferey et al claimed that C5-C9 hydrocarbon adsorbs efficiently with the MIL-53 (Cr) at low pressure due to strong host–guest interaction [25]. Albero et al found that the adsorption of n-nonane in mesoporous carbon materials, OM-CDC offer improved kinetics in the adsorption process [26]. Xie et al showed that the adsorption of n-decane on clay minerals are significant than other aromatic C7 molecules [27]. Castellon et al separated n-alkanes (C5-C9) using Cu-volcanic glass by an inverse gas chromatographic method [28]. Larese et al claimed that longer alkanes (C8) have greater interaction with the hBN substrate [29]. Denayer et al studied the liquid phase adsorption of C5-C24 linear alkanes in zeolite 5A at 298.15 K claim that the shortest chain remains as a whole and the longer chains are get perturbed in a bent configuration and the loading

* Corresponding authors.
E-mail addresses: mohanty.biswajit72@gmail.com (B. Mohanty), gopalavashthi@gmail.com, gopal.avashthi@ppsu.ac.in (G. Avashthi).

https://doi.org/10.1016/j.rinp.2023.107016
Received 5 July 2023; Received in revised form 5 September 2023; Accepted 20 September 2023
Available online 22 September 2023

capacity reduces from lower to higher carbon chain [30]. Denayer et al studied C1-C14 n-alkanes on chabazite and SAPO-34 and claim that the adsorption enthalpy increases on the homologous series and the C7-C10 alkanes adopt coiled configuration and strongly enhances the binding enthalpy [31,32]. However, these compounds have major pitfall related to their low thermal stability, particularly in MOF. High-cost organic precursors, small pore aperture of zeolites and activated carbons which truncate their robust use in the adsorption and separation of higher n-alkanes [33,34]. Thus, the scientific community has strived to produce smart material with high porosity and cost-effective for adsorption and separation of higher hydrocarbons, interestingly C8–C12.

Hitherto, a very limited report has been published which is impotent to describe the selective adsorption and separation of higher HCs. The increase of linearity, hydrophobicity, and non-polarizability are the bottleneck for the adsorption of HCs in microporous material. For the first time, we have used a discrete tubular shaped metallocavitand system, pillarplex (PPX) synthesized by Pöthig et al claims that the organometallic host is capable to accommodate a linear guest within its cavity [35]. The organometallic host shows superiority over other metal coordinated systems by the straightforward synthesis, high solubility, tunable functionality, and high thermal stability. The major advantage of the organometallic system is the transformation of the single crystal of one morphology to another, which allows the exact monitoring of the guest orientation within the cavity of the host system, resulting in the crystalline phase transformation process [36]. The PPX molecule is an octanuclear N-heterocyclic carbene complex coordinated with the coinage metals such as Cu(I), Ag(I), and Au(I) centers and exhibiting potential stability against air and moisture. To check the host capability, the author studied 1,8-diaminooctane molecule as a model guest molecule in the Au(I) coordinated PPX and claim that the PPX is highly selective for linear molecules [35]. It has been also investigated that Au-PPX exhibits inherent luminescent properties resulting an shortening of Au–Au contacts at the excited state and upon guest encapsulation the quenching effect is observed [37]. Castro et al investigated Cu-based pyrozollate system and claimed that metallacycle host has potential advantages in comparision to their organic counterparts owing to the presence of versatile metal center that can modulate the surrounding electron density [38].

We have further investigated the PPX molecules and its host–guest behavior for the 1,8-diaminooctane by using Ag, Au, and Cu metal-centered PPX and found that the guest molecule binds ideally within the cavity with minimal deformation. Further, we have studied the system to determine the adsorption behavior of PPX towards the higher HCs. Herein we have reported HCs such as C8–C12 within the cavity of the PPX [Cu (I), Ag (I), and Au(I)] and their selective adsorption and separation have been studied using various computational approach. Recently it has been observed that Cu(I) and Au(I) metallocavitand species exhibits enhanced interaction energy suggesting the possible formation of the host–guest pairs along with the coinage metal group [39]. Hence, density functional theory (DFT) has been used to determine the electronic structure and stability of the PPX and n-HC encapsulated PPX complex [40]. Natural bond orbital (NBO) analysis has been carried out to provoke the charge transfer mechanism between the intramolecular host–guest complex [41]. The nature of interaction has been deciphered by the noncovalent index (NCI) analysis [42]. The contribution of interaction has been quantified by using an energy decomposition analysis (EDA) scheme [43]. The maximum loading of hydrocarbon has studied using the Grand canonical Monte Carlo (GCMC) simulation and the adsorption enthalpy also known as isosteric heat of adsorption (Q_{st}) has been analyzed to study the thermodynamic stability of the system [44,45]. The selective separation of one component of HCs over the multicomponent mixtures has been studied using an ideal adsorption solution theory (IAST) method [46].

Computational details

The initial crystal structure of Au(I) coordinated PPX has been obtained from reference [35] and afterward Ag(I) and Cu(I) seamed PPX has been modeled by replacing the Au center. The structures are optimized using B3PW91 functional and Los Alamos double ξ effective core potential basis set LanL2DZ [47,48]. The choice of basis set and functional is in accordance with the antecedent data published by Peel et al which shows reasonably accurate results for the coinage metal on a comparison of their minimum root mean square percentage (RMS%) error [49]. The long-range interaction effect has been studied by incorporating the Grimme's dispersion D3 term [50]. HCs, C8–C12 encapsulated PPX (M = Cu, Ag, and Au) complexes has been optimized using the same level of theory. Subsequent frequency calculation has been carried out to determine the stability of the complex. The presence of real value of frequency in the minima of the potential energy surface proclaims the obtained geometry is in the ground state. The binding energy and the zero points corrected binding energy (ZPE) has been calculated for the host–guest system, subsequently, the basis set superposition corrected binding energy (BSSE) has been computed using the supermolecular approach proposed by Boys and Bernadi [51]. All the DFT computations have been carried out using the Gaussian 09 programme package [52].

The existence of intramolecular charge transfer within the complex has been studied by performing the NBO analysis [53]. The real space visualization of weak interaction has been analyzed using the noncovalent interaction (NCI) index [42]. The nature of interaction in the host–guest complex can be broadly understood by investigating electron density, ρ(r) and the reduced density gradient (RDG), s(r), a dimensionless quantity describes the deviation from the homogeneous electronic distribution as given in the Eq. (1).

$$s(r) = \frac{1}{2(3\pi^2)^{1/3}} \frac{|\nabla\rho(r)|}{\rho(r)^{4/3}} \quad (1)$$

The reduced gradient s(r) is very small and approaches to zero (≈0) for both covalent and noncovalent interactions. low-density low gradient region is obviously related to the noncovalent interaction probably van der Waals type, whereas the higher density is the stronger interaction. Although the localization of electron density enables the covalent and noncovalent interaction in a molecular host–guest system but remain silent on more specific interaction. The Laplacian of the density, $\nabla^2\rho(r)$, is a versatile tool to distinguish the different types of strong interactions [54]. Laplacian is the sum of eigenvalues of the electron density Hessian matrix along the three principal axes of maximal variation as follows;

$$\nabla^2\rho(r) = \lambda_1 + \lambda_2 + \lambda_3 \quad (2)$$

At nuclei, all three eigenvalues are negative and the density reaches local maxima. In the case of the strong covalent interaction, the Laplacian is negative whereas in weaker noncovalent interaction the Laplacian in the interatomic region is dominated by the positive contribution. If the atoms are in the bonded contact the value of eigenvalue $\lambda_2 < 0$ while in non bonded contact the $\lambda_2 > 0$ in the interatomic region [54]. Therefore the sign of the value of λ_2 can able to distinguish the nature of the interaction. Thus, analysis of the sign of λ_2 (sign(λ_2)) helps to discern different types of weaker noncovalent interactions present in the host–guest complex system [55]. Multiwfn programme suit has been used to perform the NCI index with the previously obtained wavefunction [56]. The color of the isosurface blue and green depicts the attractive hydrogen bonding and van der Waals interaction respectively while the red color present mostly in the ring center represents the repulsive steric clashes according to the present color coding scheme.

The quantitative energy terms, which are the responsible factor for the guest binding in the host–guest system is revealed via the EDA

scheme. The dispersion D3 corrected EDA calculation has been performed at B3LYP and triple zeta double polarization TZ2P level of theory using ADF (2017) program package [57,58]. Zeroth order regular approximation (ZORA) with the scalar relativistic method has been invoked during the computation as coinage metal Cu, Ag, and Au exhibits the larger relativistic effect [59]. In EDA the total interaction energy is decomposed into attractive electrostatic (ΔE_{elct}), dispersion (ΔE_{disp}), orbital (ΔE_{orb}) and the repulsive Pauli's (ΔE_{Pau}) interaction. The ΔE_{elct} gives the information about electrostatic interaction exist between the two interacting fragments by the electron density distribution in the complex system. ΔE_{disp} is the dispersion interaction is a quantum mechanical assumption which emerges due to the density fluctuations between the interacting fragments (host and guest). ΔE_{orb} is the orbital interaction occurs probably by the interaction of the occupied orbital of one fragment with the unoccupied orbital of another fragment. ΔE_{Pau} is Pauli's repulsive term appears as the overlap of two occupied orbitals in the same region of space [43,60].

The gravimetric estimation of adsorption of C8–C12 hydrocarbons has been studied using Grand canonical Monte Carlo (GCMC) simulation. The simulation has been carried out in a $2 \times 2 \times 2$ supercells with the cell dimension of $59.154 \times 46.344 \times 28.317$ Å. All GCMC simulations are performed at 273, 298, 323 and 350 K and the pressure range lies from 0.1 to 50 bar. Universal force field (UFF) parameters are used for the Lennard-Jones (LJ) potential [61]. The Ewald summation method and a 12.5 Å cut-off distance are set for the LJ interaction. The simulation carried out at 1×10^5 equilibrations and by production run and each cyclic run intends random moves such as translational, rotational, insertion and deletion with a probability of 0.20. Each. The number of adsorbed molecules fluctuates during the simulation run of each cycle and for every change of physical variables such as temperature and pressure [62]. The thermodynamic stability of the bulk system has been further analyzed by using the isosteric heat of adsorption (Q_{st}) obtained from the GCMC calculation. A negative value of Q_{st} represents the thermodynamic stability of the system for n-HCs adsorption.

The selectivity of the one component over the multicomponent mixtures has been analyzed using the ideal adsorption solution theory (IAST) method proposed by Myers and Prausnitz [63]. Various adsorption models have been validated and Brunauer-Emmett-Teller (BET) Isotherm model has been fitted more precisely with the R^2 value of 0.99 and the equation is given as follows [64].

$$n(p) = \frac{q \times K1 \times P}{(1 - K2P)(1 + (K1 - K2) \times P)} \quad (3)$$

Where P is the pressure of the bulk gas at equilibrium, n(p) is the gas uptake, q is the saturation capacities. k1 and k2 are the affinity coefficients of the sites.

Results and discussion

Geometry and energetics

The Cu, Ag and Au seamed PPX structures have been optimized and the structures are shown in Fig. S1, supporting information. The experimental crystal structure explores the height of the metallocavitand approximately 11.700 Å, the Au–Au distances 3.005 (approx.) and the inner cavity distance measured between the opposite $–CH_2$ and –CH of pyrazole unit are approximately 9.628 and 8.541 Å respectively. The metal seamed optimized structure reveals the height of Ag-PPX is 11.923 Å is higher than the Cu and Au-PPX and the Ag–Ag distance is 3.095 Å which is slightly higher than Au–Au (3.094) distances while the Cu–Cu distances are 2.945 Å. The inner cavity distance measured between the opposite face of $–CH_2$ unit decreases from Cu (10.059) to Au (9.900) whereas the opposite faced –CH of the pyrazole unit is increased gradually from Cu (8.379) to Au (8.539). The experimental structure is well agreement with the optimized Au-PPX structure. Hence the B3PW91-D3/LanL2DZ level of theory is ideal to study the coinage metal coordinated complex structure and their host–guest behavior.

A comprehensive analysis has been carried out to understand the hydrocarbon viz. C8–C12 adsorption within the cavity of the Cu, Ag, Au seamed PPX. The guest hydrocarbons are linear and lengthy, so vertical orientation is the only possibility of residing within the cavity of the PPX. The observed chain length of guest, measured between the two terminal carbon atom, after complexation, is lower than the pristine guest is given in Table 1. The pristine chain length of C8, C9, C10, C11, and C12 are 9.016, 10.257, 11.574, 12.823 and 14.135 Å respectively. The chain length of the guest is lower in Cu-PPX and higher in Ag-PPX while a contrary observation is observed for C12 encapsulated Ag-PPX where the chain length of C12 (14.035 Å) is lower than the Cu (14.052 Å) and Au-PPX (14.062 Å). The shorter chain length of C12 in Ag-PPX can be understood by the structure curvature. The reduction of chain length in the guest encapsulated PPX structures compels the contraction of C-C bond length within the complex is due to the metal-hydrogen (HCs) interaction. The measured average bond distance between the Cu–Cu, Ag–Ag, and Au–Au in the PPX is 2.945, 3.095 and 3.094 and the guest encapsulated PPX depicts a decrease in the metal–metal bond distances which reveals metal-guest interaction. The Ag–Ag and Au–Au distances are below the sum of their van der Waals radii (3.4 Å for Ag–Ag and 3.2 Å fo Au–Au) depicting the argentophilic and aurophilic interactions, respectively, whereas the Cu–Cu van der Waals radii lies 2.8 Å, hence no cuprophilic interactions observed. Such closed shell attraction plays crucial role in the geometrical and electronic structural diversity including many potential applications in material science to catalysis and medicinal chemistry. The Cu–Cu distance in C8@Cu-PPX is 2.916 Å and it decreases substantially upon the increasing chain length and becomes 2.910 Å in the C12@Cu-PPX complex. The metal–metal bond distances are given in Table 1. Likewise, the Ag–Ag bond distance in C8@Ag-PPX is 3.071 Å and the C12@Ag-PPX is 3.066 Å and the Au–Au bond distance in C8@Au-PPX is 3.074 Å and C11@Au-PPX is 3.074 Å. contrarily, the average Au–Au distance in C12@Au-PPX is 3.082 Å is slightly higher than other hydrocarbons.

A rational interaction of –CH of an HCs with the -N atom of pyrazole, imidazole, and metal (Cu, Ag, Au) center has been investigated. For simplicity, we have considered the minimum distance of –CH···X (X = N, Cu, Ag, Au) interaction and the distances are shown in Table S1, supporting information. The –CH···N (pyrazole) distance in HC@Cu-PPX is 2.734–2.777 Å and –CH···N (imidazole) distance is from 3.088 to 3.000 Å. The –CH···N (imidazole) distance decreases from C8 to C12. In

Table 1
The distance between the M–M center (d_{M-M}), the distance between the two terminal carbon of the encapsulated guest ($d_{encap.\ HC}$), deformation energy (DE) of host and guest of the HC encapsulated PPX system. The DE is measured in kcal/mol whereas distances are in Å unit.

System	d_{M-M} (Å)	$d_{encap.\ HC}$ (Å)	DE (Host)	DE (Guest)
Cu-PPX	2.945	–	–	–
C8@Cu-PPX	2.916	8.963	1.37	0.21
C9@Cu-PPX	2.911	10.174	1.52	0.26
C10@Cu-PPX	2.914	11.514	1.63	0.24
C11@Cu-PPX	2.914	12.740	1.70	0.28
C12@Cu-PPX	2.910	14.052	1.62	0.37
Ag-PPX	3.095	–	–	–
C8@Ag-PPX	3.070	8.972	0.46	0.17
C9@Ag-PPX	3.069	10.198	0.56	0.18
C10@Ag-PPX	3.067	11.529	0.63	0.19
C11@Ag-PPX	3.068	12.760	0.82	0.21
C12@Ag-PPX	3.065	14.035	0.65	0.65
Au-PPX	3.094	–	–	–
C8@Au-PPX	3.074	8.966	0.87	0.18
C9@Au-PPX	3.072	10.205	0.93	0.17
C10@Au-PPX	3.074	11.524	0.89	0.20
C11@Au-PPX	3.074	12.744	0.98	0.24
C12@Au-PPX	3.082	14.062	0.98	0.30

HC@Ag-PPX, the –CH···N (pyrazole) interaction distances are lies in 2.750–2.791 Å while the –CH···N (imidazole) distance is 3.021–2.936 Å. The interaction distance of –CH···N (pyrazole) in HC@PPX is 2.760 to 2.822 and the value decreases from C8 to C12 but in –CH···N (imidazole), no such pattern is observed. The –CH···N (imidazole) distance is in the range of 2.998 to 3.051 Å. In each case, the –CH···N interaction reveals a moderate hydrogen bonding interaction, mostly of electrostatic in nature. Further we have shown interest in the M···H interaction. The –CH···Cu, –CH···Ag and –CH···Au distances vary from 2.634 to 2.662, 2.688–2.719 and 2.716–2.778 Å. The interaction of Cu(I), Ag(I), and Au(I) with the HCs at a noticeable bond length clearly enunciates stronger than normal van der Waals interaction [65].

A meticulous analysis of deformation energy (DE) provides an insight into the alteration in physical properties of guest and host after the complexation. The DE of the guest is lower than the host molecules and the guest molecules within the Cu-PPX manifests higher deformation than Ag and Au-PPX. The DE of each host guest energies is given in Table 1. The increasing length of the guest results in higher DE. The DE of C8 in Cu-PPX is 0.21 kcal/mol, whereas in Ag and Au-PPX is 0.17 and 0.18 kcal/mol. In C12, the DE of Ag-PPX is 0.65 kcal/mol is higher followed by Cu-PPX (0.37 kcal/mol) and Au-PPX (0.29 kcal/mol). The higher DE of C12 in Ag-PPX is due to the curvature effect. The unlikely guest molecule, host PPX shows potential deformation after complexation and the ease of deformation is higher in the Cu-PPX followed by Au-PPX and Ag-PPX. The magnitude of the DE in Cu-PPX from C8 to C12 lies in the range of 1.37 to 1.70 kcal/mol where for Ag-PPX and Au-PPX the energy term is in the range of 0.46–0.82 and 0.87–0.98 kcal/mol respectively. The DE of Ag-PPX in the C12 complex is lower than the C11 complex is due to the higher deformation of the guest. The DE of both host and guest is competently notable, which preambles the guest binding affinity of PPX and the higher DE associated with Cu-PPX could have prominent binding efficiency.

The binding energy (ΔE) of each guest encapsulated PPX has been investigated with contemplating long-range interaction. The ΔE of the guest is higher for Cu-PPX and lower in Ag-PPX and the energy values are given in Table 2. The ΔE of C8, C9, C10, C11 and C12 in Cu-PPX is −58.13, −60.57, −62.45, −63.94 and −64.98 kcal/mol respectively whereas the ΔE of C8, C9, C10, C11, and C12 in Au-PPX is −54.68, −57.44, −59.64, −61.21 and −62.51 kcal/mol is 3.65, 3.52, 3.61, 3.48, and 3.75 kcal/mol higher than the Ag-PPX. The higher binding energy denotes the stabilization by considering the linear shape of the guest. The host–guest complexes are shown in Fig. 1. The higher binding energy of the guest with PPX can be understood by the Pearsons hard soft mechanism. The coinage metal cation Cu (I), Ag (I) and Au (I), all belong to the soft acid and the long chain HCs also act as a soft base and the magnitude of softness is higher for Au (I) followed by Ag (I) and Cu (I), hence the ΔE of guest@PPX is exceptionally higher. Further, we have computed ZPE corrected binding energy, reveals no pragmatic change in the binding energy whereas a substantial change in BSSE corrected energy reveals the basis function overlap exert in the complexation process. The stability of the PPX and the guest encapsulated PPX has probed by computing frequency analysis enumerated by the presence of real frequency values in the optimized geometry. The negative Gibbs free energy (ΔG) values portray the guest@PPX is spontaneous and feasible at ambient condition, supported by enthalpy (ΔH) change is given in Table 2. The ΔG value for C8 to C12 in Cu-PPX is in the range of −42.05 to −49.73 kcal/mol and the ΔH value varies from −56.65 to −63.71 kcal/mol and the increasing HC chain length leads a higher thermodynamic property. The same vogue is observed for the guest adsorption in Ag-PPX and Au-PPX. The $\Delta G_{298.15}$ value in Ag-PPX is −35.14 to −41.55 kcal/mol whereas in Au-PPX is −38.80 to −46.29 kcal/mol for C8 to C12 hydrocarbon respectively. The ΔH swings from −49.32 to −57.01 kcal/mol in Ag-PPX and −52.95 to −60.72 kcal/mol in Au-PPX for C8–C12 claims the adsorption of HCs within the PPX are stabilized by the enthalpic process. Among Cu, Ag and Au-PPX complex, the ΔG and ΔH value are found higher for Cu-PPX followed by Au-PPX and Ag-PPX is lower among all, hence the adsorption and separation is more facile in Cu-PPX complex followed by Au-PPX. The effect of entropy is negligible small over various complexes. The ratio of $\Delta H_{298.15}$ in C12/C11, C11/C10, C10/C9, C9/C8 lies above 1.00, which depicts the possibility of separation of the desired HCs from their multicomponent mixture.

The electronic mechanism has been investigated by computing the frontiers molecular orbital (FMO) analysis. In Cu-PPX, the highest occupied molecular orbital (HOMO) remains conserved throughout the HCs adsorption as shown in Fig. 2. However; a significant change in the lowest unoccupied molecular orbital (LUMO) was observed in the adsorption process, which portrays the contribution is favoured from the LUMO of the PPX. From the FMO claculations it is evident that LUMO showed a pσ bonding orbital linked with the interacting metal atoms (Cu, Ag, Au), accompanied by additional contributions from the adjacent N-atoms p-orbitals. The HOMO of the PPX consists of metal d- and pyrazole π*-orbitals and is highly localized in the d-orbitals of metals and this features are observed for all the systems.The bidirectional charge transfer occurred between HCs C-H group and the metal center. The energy gap increses from the C8 to C11 while the C12 have lower energy gap compared to the C11. A similar trend is observed for the Ag-PPX system while in Au-PPX an anomaly has shown and the change in energy gap is not well pronounced as shown in Fig. S2, supporting information. The computed E_{gap} (energy difference between the HOMO and LUMO is higher for Ag-PPX (5.21 eV) implies high kinetic stability and low chemical reactivity and Au-PPX is 4.79 eV reveals high chemical reactivity. Hence the guest adsorption is facile towards the Au-PPX and Cu-PPX than Ag-PPX. Upon adsorption of guest molecules within the cavity of PPX,

Table 2
The binding energy (ΔE) of the guest adsorbed by PPX, zero-point corrected binding energy, basis set superposition corrected (BSSE) binding energy, change in free energy ($\Delta G_{298.15}$), change in enthalpy ($\Delta H_{298.15}$) and change in entropy ($\Delta S_{298.15}$). The energy values are expressed in kcal/mol.

System	Binding energy (ΔE)	Zero-point corrected ΔE	BSSE corrected ΔE	$\Delta G_{298.15}$	$\Delta H_{298.15}$	$\Delta S_{298.15}$
C8@Cu-PPX	−58.13	−56.84	−45.61	−42.05	−56.65	−0.05
C9@Cu-PPX	−60.57	−59.58	−49.10	−45.83	−59.21	−0.04
C10@Cu-PPX	−62.45	−61.63	−50.74	−47.60	−61.18	−0.04
C11@Cu-PPX	−63.94	−62.94	−51.84	−48.55	−62.55	−0.04
C12@Cu-PPX	−64.98	−64.11	−54.25	−49.73	−63.71	−0.04
C8@Ag-PPX	−51.03	−49.56	−42.36	−35.14	−49.32	−0.04
C9@Ag-PPX	−53.92	−52.25	−44.65	−37.38	−52.06	−0.05
C10@Ag-PPX	−56.03	−54.59	−46.39	−39.39	−54.35	−0.05
C11@Ag-PPX	−57.73	−55.92	−47.68	−40.61	−55.73	−0.05
C12@Ag-PPX	−58.75	−57.20	−48.52	−41.55	−57.01	−0.05
C8@Au-PPX	−54.68	−53.20	−45.57	−38.80	−52.95	−0.05
C9@Au-PPX	−57.44	−55.88	−47.71	−41.67	−55.60	−0.05
C10@Au-PPX	−59.64	−57.77	−49.52	−42.19	−57.65	−0.05
C11@Au-PPX	−61.21	−59.36	−50.74	−43.48	−59.22	−0.05
C12@Au-PPX	−62.51	−61.00	−51.82	−46.29	−60.71	−0.05

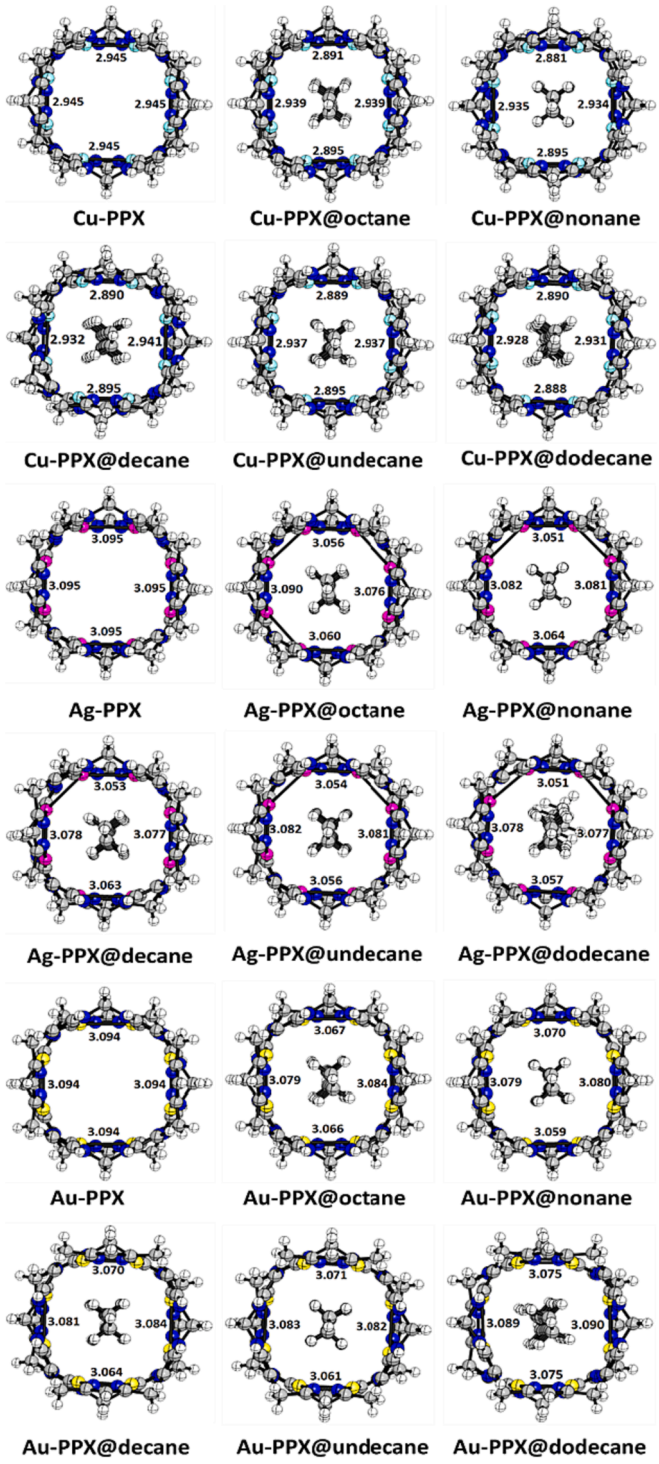

Fig. 1. The optimized geometry of HC (C8–C12) encapsulated PPX complex. The cyan, magenta, gold, blue, grey and white color balls represent the Cu, Ag, Au, N, C and H atoms. The M–M (Cu, Ag, Au) bond lengths are inset. (For interpretation of the references to color in this figure legend, the reader is referred to the web version of this article.)

To discern the reactivity of the different PPX, we evaluate the global descriptors such as electronegativity (χ), hardness (η), and electrophilicity index (ω) in conceptual density functional theory framework, the theoretical concept has been briefed in supporting information. The electronegativity of Ag-PPX is 11.84 eV is higher than Cu (11.82 eV) and Au-PPX (11.80 eV) conveys the Ag-PPX shows a higher affinity towards the HCs for adsorption interaction than Cu and Au-PPX. The maximum hardness principle (MHP) and minimum electrophilicity principle reveal the Ag-PPX is highly stable as it exists a higher η and lower ω value and Au-PPX shows higher ω and lower η value represents the higher reactivity of the system. The order of reactivity is Au-PPX > Cu-PPX > Ag-PPX. the magnitude of χ, η, and ω decreases while he E_{gap} value decreases, implicating a stable host–guest complex. Further, we have computed N_{max}, the maximum number of electrons that an electrophile can acquire imputes the Au-PPX to have a higher tendency of 4.92 e^- followed by Cu-PPX (4.84 e^-) and Ag-PPX (4.54 e^-) illustrates that the Au-PPX is prominent for guest adsorption followed by Cu-PPX. The global descriptors, $E_{gap,}$ and N_{max} against the binding energy are given in Fig. 3.

Nature of interaction

NBO charge analysis

Intramolecular charge transfer in the complex provides significant insight of host–guest interaction by computing the electronic transfer, occurs on the electrophilic site. In comparison with the Cu, Ag, and Au-PPX, the magnitude of charge transfer from the metal center is higher in Cu-PPX (0.554 e^-) than Ag-PPX (0.527 e^-) and Au-PPX (0.399 e^-). The lower charge contribution in Au can be of high relativistic effect. The addition of guest viz. C8, C9, C10, C11, and C12 within the PPX show a slight decrease in charge transfer than the pristine PPX while from C8 to C12@PPX, the contribution of electronic transfer from the metal site is very persistent. The charge transfer in HC@Cu-PPX is 0.548 e^-, while in Ag-PPX and Au-PPX is ca. 0.513 and 0.377 e^- respectively from the metal centre as shown in Table S2, supporting information. Additional 0.005, 0.014 and 0.022 e^- transfer occurs after the encapsulation of HCs within the Cu, Ag, and Au-PPX respectively. A notable change in the electronic transfer prevails in guest HCs, where the extent of charge transfer lies in the range of 0.161–0.169 e^-, 0.160–0.168 e^-, and 0.154–0.158 e^- from C8–C12 to Cu-PPX, Ag-PPX, and Au-PPX respectively. The HCs within the cavity of Cu-PPX shares the maximum number of electrons while in Au-PPX the sharing of electrons is minimum. The maximum electronic transfer in the host–guest system reveals the higher binding affinity, which unveils from their binding energy value.

Noncovalent interaction

To decipher the nature of the interaction, we have performed the noncovalent index (NCI) analysis which portrays the spectrum of weak interactions in the host–guest systems and the plot is shown in Fig. 4. The NCI analysis portrays a green isosurface is surrounding the guest HCs within the PPX cavity conveying the van der Waals type of interaction exerted between the host PPX and the guest HCs. A red color spattered plot is visualized in the ring center of pyrazole and imidazole ring center reveals the repulsive forces exist by the ring strain. A blue color fleck is present between the M(I)-M(I) (M = Cu, Ag, Au) center revealing strong attractive metallic bonding interaction exist therein. The increasing chain length of the HCs results in the increase of van der Waals surface around the HC chain. From NCI- isosurface analysis, it is coherent that the host–guest interactions in HC@PPX are van der Waals type. For better understanding, we have analyzed the reduced density gradient, *s* versus sign $(\lambda_2)\rho$. In the reduced density plots, the very low density, low gradient troughs with negative sign $(\lambda_2)\rho$ values indicates the dispersion interaction, whereas moderately low density and low gradient represent the strong attractive interaction. Contrarily a positive value of low density and low gradient at the right side of the sign $(\lambda_2)\rho$ designate the strong repulsive interaction exerted by steric clashes. A superimposed plot *s* versus sign $(\lambda_2)\rho$ of PPX (red in color) and the guest encapsulated PPX (blue in color) has been shown in Fig. S3, supporting information. In each system, an extra trough appears highlighted with green rectangle boxes, with slight negative sign $(\lambda_2)\rho$ values around −0.005 a.u., which implies the guest molecules bound with the host by dispersive interaction. The *s* value of 1.3 a.u. in Cu-PPX implies that the

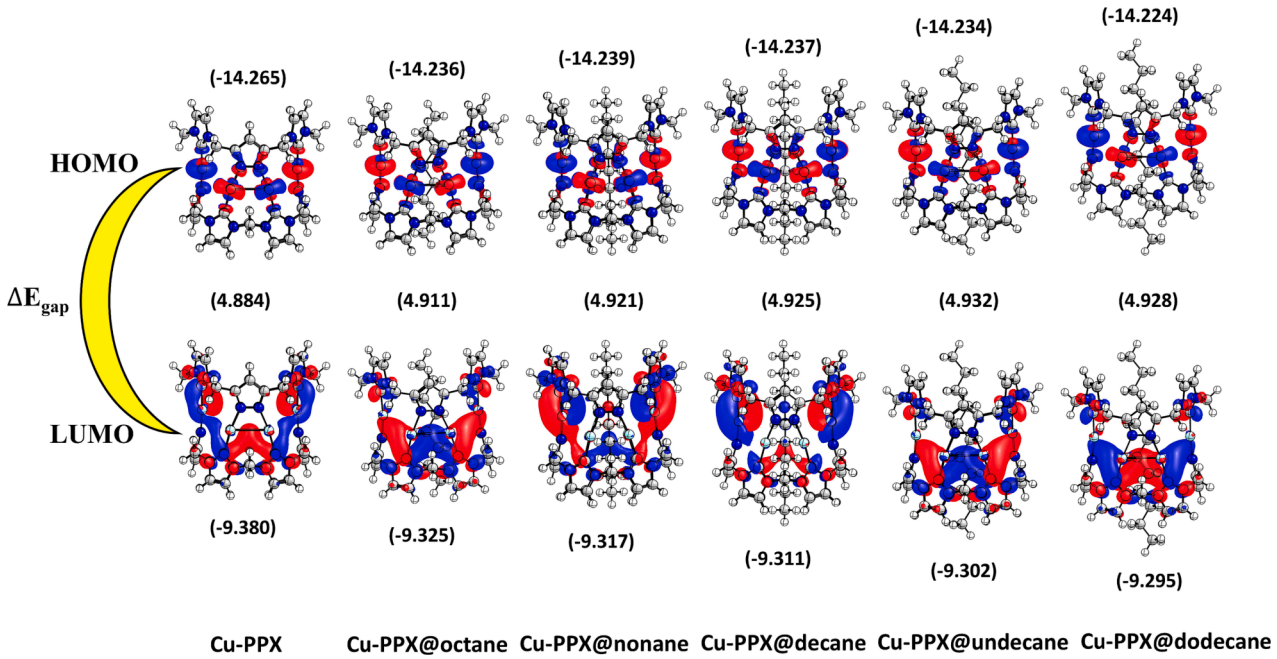

Fig. 2. The frontier molecular orbital diagram of highest occupied molecular orbital (HOMO) and lowest unoccupied molecular orbital (LUMO) and Energy gap (E_{gap}) is the energy difference between the HOMO and LUMO. The energy terms are given in the electron volt (eV) units.

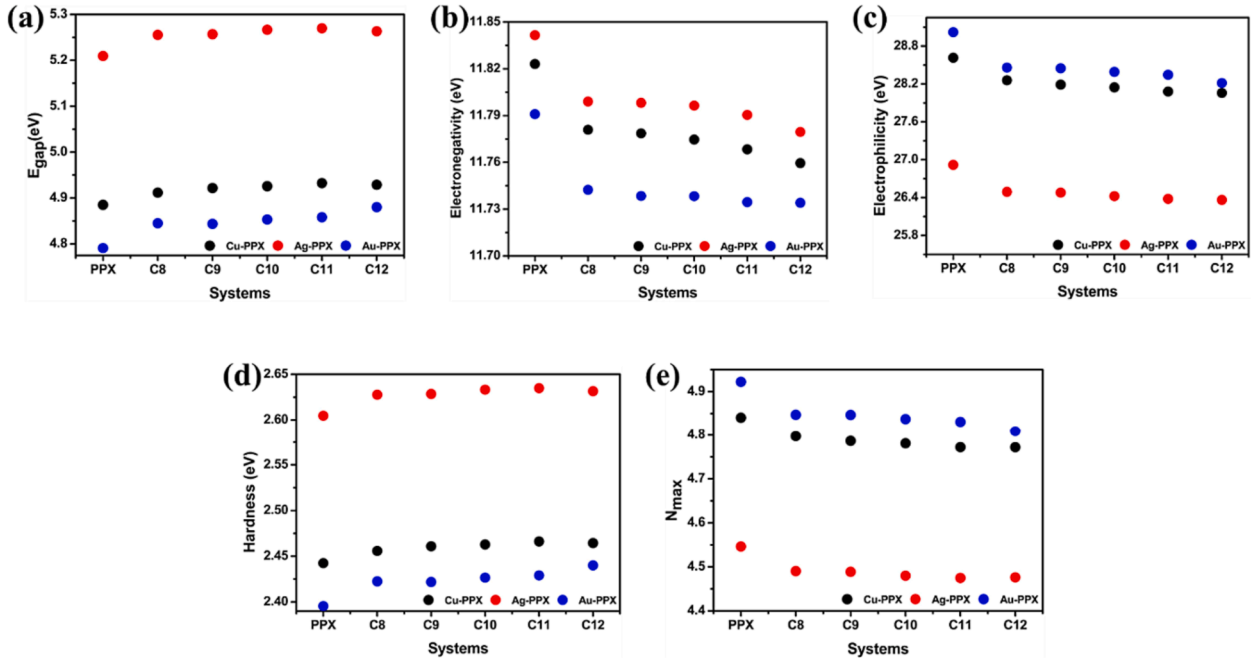

Fig. 3. The conceptual DFT parameters (a) Energy gap (E_{gap}) is the energy difference between the HOMO and LUMO, (b) electronegativity, (C) electrophilicity (d) hardness and (e) the N_{max} represents the maximum number of the electron that an electrophile can acquire. The energy terms are given in the electron volt (eV) units.

HCs have higher interaction contact within the Cu-PPX followed by Au- and Ag-PPX (ca.1.2 a.u.). The ease of attractive interaction is higher in Au-PPX (sign $(\lambda_2)\rho = -0.03$) followed by Ag-PPX (sign $(\lambda_2)\rho = -0.02$) and Cu-PPX (sign $(\lambda_2)\rho = >-0.02$), this could be understood by the increasing softness of the metal center having a higher tendency to bind soft HCs. The repulsion in Au-PPX is higher than corresponding Ag-PPX and Cu-PPX is due to the maximum orbital overlap of M–M center.

Energy decomposition analysis

The NCI analysis gives a strong background of attractive and repulsive interaction but remains silent about the quantitative stockpile, therefore to understand the relative contribution of attractive terms viz. ΔE_{elct}, $\Delta E_{disp,}$ and ΔE_{orb} towards the total binding strength, ΔE. The EDA has been performed by taking each host and guest as individual fragments. The energy components are given in Table 3 along with the percentage of contribution of individual terms to the total binding energy. EDA analysis reveals the major energy components responsible for the adsorption of HC is dispersion energy, ΔE_{disp} is around 59–62% in all the systems. The high dispersion term can be easily understood that being the tubular shape of host the HCs within the cavity maximizes the

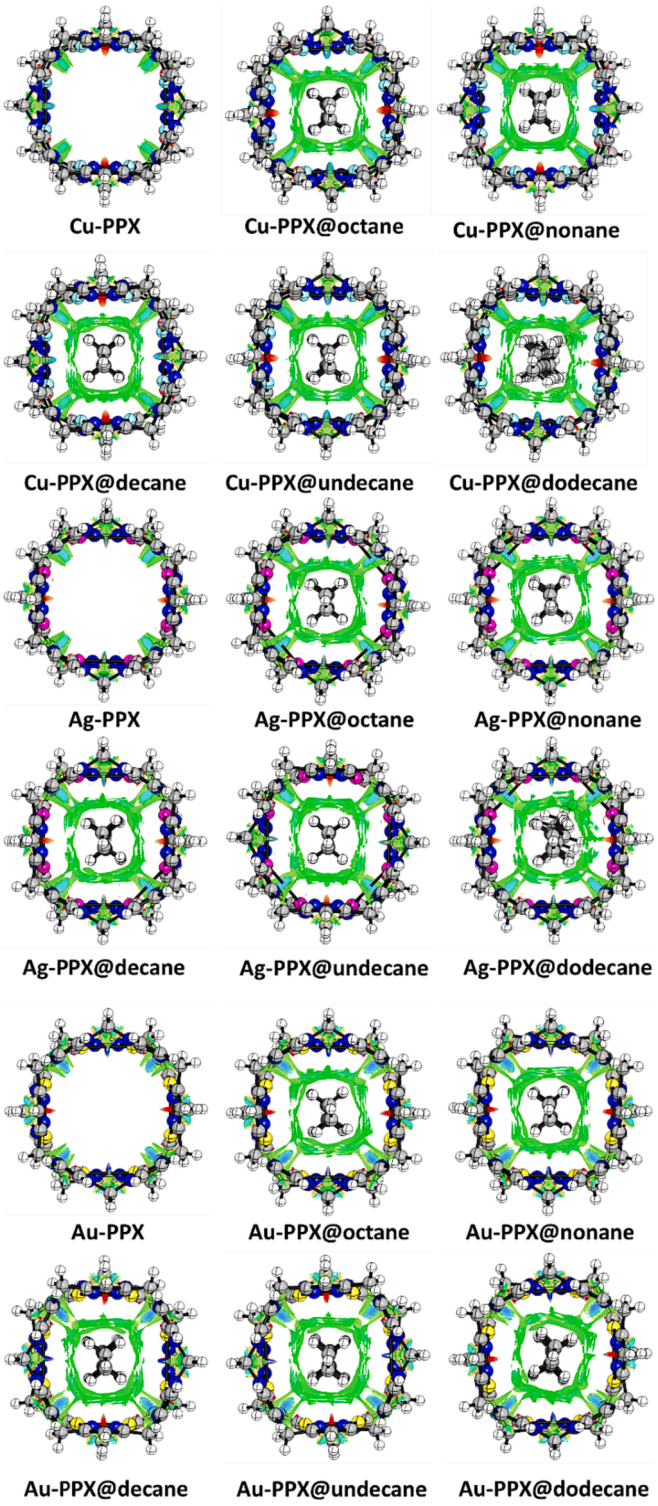

Fig. 4. The noncovalent interaction plot of HC encapsulated PPX, the green spattered region depicts the van der Waals type of interaction, The repulsive interaction is shown by the red fleck. (For interpretation of the references to color in this figure legend, the reader is referred to the web version of this article.)

surface contact with the PPX. In addition to the electron correlation strengthened by the relativistic effect played an essential role and the Cu (I)-Cu(I), Ag(I)-Ag(I), and Au(I)-Au(I) interaction was attributed to the London dispersion effect and such attractiona are remarkably stronger than the normal van der Waals interactions [65]. The contribution of

Table 3
The percentage of contribution of electrostatic interaction energy (ΔE_{elct}), dispersion energy (ΔE_{disp}), orbital interaction energy (ΔE_{orb}) and the repulsive Pauli's energy (ΔE_{Pau}) in the host–guest complex. The energy terms are in kcal/mol unit and shown in the parenthesis.

System	ΔE_{elct}	ΔE_{disp}	ΔE_{orb}	ΔE_{Pau}
C8@Cu-PPX	24.35(−24.41)	60.32(−60.47)	15.33(−15.37)	52.31
C9@Cu-PPX	23.83(−24.65)	60.84(−62.93)	15.33(−15.86)	53.16
C10@Cu-PPX	23.32(−24.74)	61.34(−65.09)	15.34(−16.28)	54.34
C11@Cu-PPX	23.29(−25.27)	61.28(−66.49)	15.43(−16.75)	55.07
C12@Cu-PPX	23.06(−25.51)	61.34(−67.89)	15.60(−17.27)	56.44
C8@Ag-PPX	24.54(−22.18)	59.81(−54.07)	15.65(−14.15)	48.5
C9@Ag-PPX	23.70(−22.32)	60.61(−57.10)	15.69(−14.79)	50.34
C10@Ag-PPX	23.71(−23.22)	60.71(−59.44)	15.58(−15.25)	51.79
C11@Ag-PPX	23.03(−22.96)	61.25(−61.07)	15.72(−15.67)	52.54
C12@Ag-PPX	24.31(−25.70)	59.74(−63.16)	15.95(−16.86)	56.42
C8@Au-PPX	23.51(−22.57)	60.64(−58.20)	15.85(−15.21)	49.95
C9@Au-PPX	22.93(−22.94)	61.13(−61.15)	15.94(−15.94)	52.25
C10@Au-PPX	22.77(−23.62)	61.29(−63.56)	15.94(−16.53)	54.06
C11@Au-PPX	22.39(−23.73)	61.58(−65.28)	16.03(−16.99)	54.92
C12@Au-PPX	23.08(−25.22)	61.03(−66.69)	15.89(−17.36)	55.57

electrostatic, ΔE_{elct} is moderate ca. 22–24% and the orbital contribution, ΔE_{orb} is ca. 15–16% which is moderately low, therefore it can't be negligible. The ΔE_{orb} term involves the polarization regions at the nearby amino groups and in a minor amount at the HC chain hydrogen atoms. The contribution of ΔE_{elct} in C8@Cu-PPX is 24.35%, reduces to 23.06% in C12@Cu-PPX while the ΔE_{disp} and ΔE_{orb} increases from C8 to C12. The ΔE_{disp} and ΔE_{orb} value of C8 and C12@Cu-PPX are 60.32 and 15.33% increases to 61.34 and 15.60% respectively. Increasing the chain length of guest in Cu-PPX deduce the lower ΔE_{elct}, higher $\Delta E_{disp,}$ and ΔE_{orb} contribution. An irregular pattern is observed for the HC@Ag-PPX complex where the ΔE_{disp} contribution of C8 is 59.81% and it increases steadily to 61.25% in C11 and for C12 it reduces to 59.74%, similarly, another unusual behavior is observed for C10, where the ΔE_{orb} contribution is slightly lower than C9 complex. The ΔE_{elct} value decreases gradually from C8 to C11 and in C12 an elevated value of ca.24.31% is observed. The convoluted interaction in Ag-PPX is due to the higher E_{gap} (E_{HOMO} − E_{LUMO}) subtle a lower adsorption contact therein the cavity other than C12, because of higher deformation stronger dipolar interaction of C12 chain. The Au-PPX follows a similar fashion like Cu-PPX. The C8@Au-PPX is 23.51% and reduces to 22.39% in C11@Au-PPX whereas the $\Delta E_{disp,}$ and ΔE_{orb} varies from 60.64 to 61.58% and 15.85–16.03% respectively. A contrary effect is observed for the C12@Au-PPX, this can be understood by the moderate hydrogen bonding interaction between the –CH atoms of C12 chain with the -N atom of imidazole/pyrazole unit, which induces higher ΔE_{elct} (23.08%), lower ΔE_{disp} (61.03) and ΔE_{orb} (15.89). The ΔE_{disp} is higher with increasing the chain length of HCs in all cases except C12 in Ag and Au-PPX where ΔE_{elct} plays a major role. Further ΔE_{orb} analysis unveils the orbital contribution increases substantially with the increasing chain length of the guest.

GCMC simulation

The gravimetric estimation of HCs within the cavity of PPX has been analyzed using GCMC simulation varying the temperature from 273 to 350 K and the pressure from the 0.1–50 bar shown in Fig. 5. The uptake capacity of the PPX in all the systems increases slowly upon the pressure and temperature swing. From the adsorption isotherm plot, it is explicit that the adsorption capacity of Au-PPX is higher than Cu-PPX and Ag-PPX. The uptake of C8 at ambient condition (298.15 K and 1 bar) in Cu, Ag and Au-PPX is 18.01, 17.50 and 25.31 cm^3STP/g respectively. Under ambient setup, the extent of adsorption of C9, C10, C11, C12 in Cu-PPX is 12.65, 12.16, 8.27 and 6.32 cm^3STP/g, which is 2.36, 2.93, 3.41, 2.92 cm^3STP/g lower than Au-PPX and 2.43, 7.30, 3.91, 5.84 cm^3STP/g higher than Ag-PPX respectively. Raising the pressure to 50

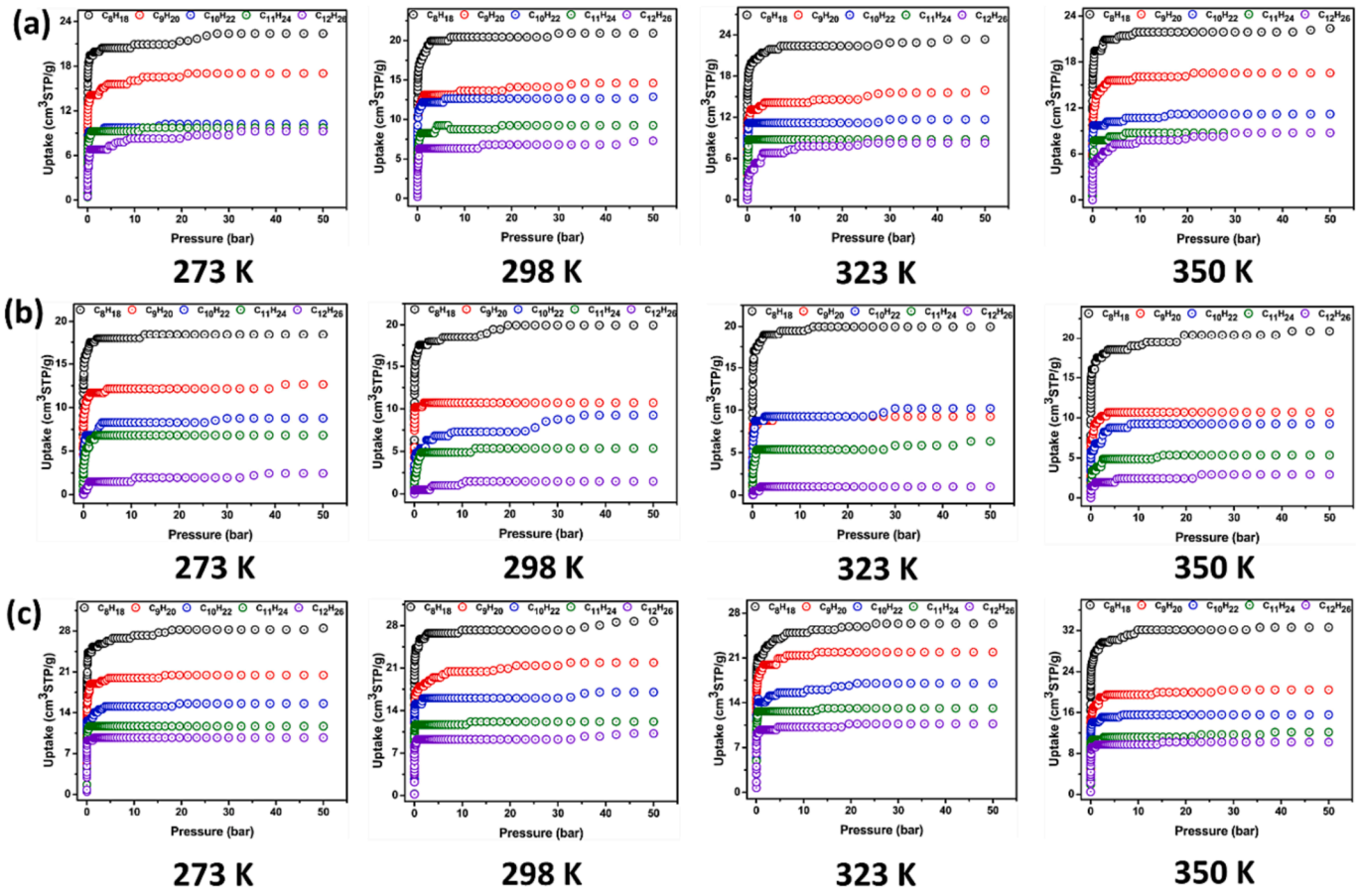

Fig. 5. The adsorption isotherm plot at various temperature and pressure from 0.01 to 50 bar using (a) Cu-PPX, (b) Ag-PPX and (c) Au-based metallocavitands.

bar at 298 K, the adsorption of C8, C9, C10, C11, and C12 in Au-PPX is 28.71, 21.90, 17.03, 12.16 and 10.22 cm^3STP/g is 7.78, 7.30, 4.16, 2.93, 2.92 cm^3STP/g and 8.76, 11.20, 7.79, 7.21, 8.76 cm^3STP/g lower than the Cu-PPX and Ag-PPX respectively. Thus for gravimetric uptake, the Au-PPX is superior over Cu and Ag-PPX system both at 1 bar and high-pressure region (50 bar) at 298 K. The adsorption of C8 at 273 K and 1 bar in Cu-PPX is 19.47 cm^3STP/g is 1.46 cm^3STP/g higher than of adsorption at ambient condition, while in Ag-PPX and in Au-PPX, the adsorption is 0.95 and 0.98 cm^3STP/g lower in quantity. Other n-HCs at 273 K and 1 bar increase slowly in the PPX system, contrarily the decane adsorption in Cu-PPX at ambient condition are higher than the present system. At 50 bar and 273 K, the adsorption of C8, C9, C10, C11, and C12 are 22.39, 17.03, 10.22, 9.73, 9.24 cm^3STP/g respectively is higher than the ambient condition but in Au-PPX, the adsorption uptake is 28.49, 20.44, 15.57, 11.68 and 9.73 cm^3STP/g is lower than ambient one. A zigzag pattern is observed for the adsorption of n-HC in Ag-PPX and also the uptake is lesser than the Cu and Au-PPX system. Further, we have studied at the higher temperature range of 323 and 350 K as the uptake capacity shows a good response to 298 K/50 bar than the 273 K/50 bar. The uptake of n-HCs at 323 K and 50 bar results in 2.43 and 0.97 cm^3STP/g higher uptake of C8 and C12 than 298 K/50 bar in Cu-PPX. C10 and C11 uptakes are 0.97 and 0.98 cm^3STP/g, which is better than the 298 K/50 bar. In Au-PPX the quantity of adsorption of C11 and C12 at 323 K/50 bar is substantially higher (<1.00 cm^3STP/g) higher than the 298 K. The C11 and C12 hydrocarbon shows an elevation with rising of temperature. At 350 K/50 bar, the uptake capacity of C9 (16.55 cm^3STP/g) and C12 (8.76 cm^3STP/g) is higher in Cu-PPX, similarly, in Ag-PPX, the adsorption of C8 and C12 is highly impressible over all the studied temperature. A dramatic preferment is observed for C8 in Au-PPX, is 32.61 cm^3STP/g, which is higher for all the studied systems. Hence GCMC simulation deduces the high temperature (323–350 K) plays the major role for the adsorption of long-chain hydrocarbons, particularly C11, and C12 in PPX complex. The gravimetric capacity of Au-PPX is higher for C8 and increases upon higher temperature (350 K/50 bar) among all the studied PPX system. Inclusive to all the Au-PPX shows notably higher uptake for n-HC followed by Cu-PPX and Ag-PPX system.

Further, we have computed isosteric heat of adsorption (Q_{st}) at 298 K/0.01–50 bar, to understand the thermodynamic aspects of guest binding. The Q_{st} value Cu-PPX, Ag-PPX and Au-PPX are varied from 19.18 to 27.86, 22.21–24.46 and 20.85–31.63 kcal/mol. The high-value Q_{st} reveals the higher binding affinity of guest with the PPX. The ratio of Q_{st} values from C8–C12 is greater than one for Au-PPX, while in Cu-PPX the ratio of C8 to other isomer is higher and in Ag-PPX, the all the Q_{st} values are in close proximity. Hence it is ideal to say that Cu and Au-PPX are better adsorber and separator for industrial application than Ag-PPX. The Q_{st} plot is shown in Fig. 6 portraying a constant value is observed for Ag-PPX upon higher uptake and pressure reveals the adsorbent (Ag-PPX) is energetically homogeneous in nature. The host Cu-PPX enunciates the stronger interaction of HCs within the cavity of PPX as the slight increase in the Q_{st} value upon increasing the pressure. The Q_{st} of C12 and C9 in Au-PPX increases steadily with the pressure results in the strong binding interaction within the cavity. The order of Q_{st} in Cu and Au-PPX is C12 > C11 > C10 > C9 > C8 at an ambient condition which is corroborated with the obtained DFT values. At higher pressure, the order of Q_{st} in Cu-PPX is C12 ≈ C10 > C11 > C9 > C8 and in Au-PPX is C12 > C8 > C11 ≈ C10 > C9, which claims the separation of C8 is superior at ambient condition and C12 is facile at higher pressure. Hence Cu-PPX and Au-PPX can be used as a potential adsorber and separator for the HC from C8–C12.

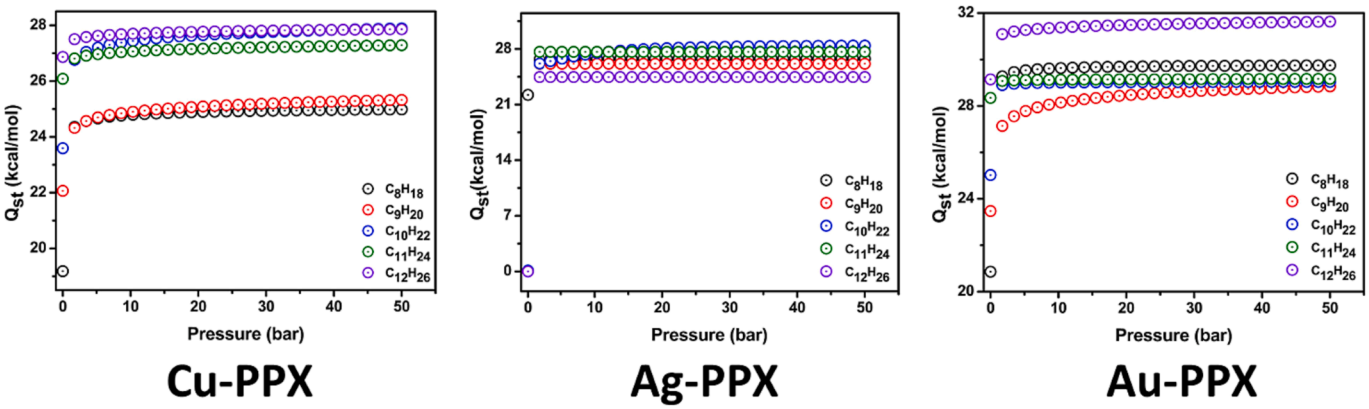

Fig. 6. The isosteric heat of adsorption (Q_{st}) at 298 K and pressure 0.01–50 bar for HC encapsulated Cu, Ag, and Au-PPX.

Ideal adsorption solution theory

The adsorption of one component from a multicomponent mixture is important for the selective separation is shown in Fig. 7 by computing the ideal adsorption solution theory (IAST) method. The IAST data reveals the higher selectivity of C8 (C_8H_{18}) among all the studied HCs, hence the separation would be more facile. At ambient condition, the selectivity of C8 is 12.33, 13.92 and 16.88 and in 298 K/50 bar is 16.27, 17.00 and 22.00 in Cu-PPX, ag-PPX, and Au-PPX respectively. The ratio of selectivity at the ambient condition of C8/C9, C8/C10, C8/C11, C8/C12 is 3.19, 5.65, 25.68, 246.6 respectively in Cu-PPX whereas in Au-PPX is 3.69, 6.37, 32.46, and 281.33 respectively. The selectivity ratio of C8/C10, C8/C11, and C8/C12 is remarkably high due to negligible selectivity of C10, C11, and C12 at ambient condition. From the above analysis, it is obvious that the C8 separation by using PPX is more prominent. Upon increasing the temperature from 298 K to 323 K, it has been observed that the selectivity of C12 and C9 achieve good selectivity in Cu-PPX and Au-PPX respectively. Hence it is straightforward to separate C9 and C12 after the complete separation of C8 from the mixture. Ag-PPX doesn't show any significant selectivity of HCs other than C8, at 2.5 bar and 298 K the C9 selectivity (2.88) is viable and at a pressure of <1 bar, there will be the possibility of separate C9, once C8 is completely removed from the system. The C12 selectivity in Cu-PPX at 323 K/50 bar is 1.84, so the practical separation is possible from other

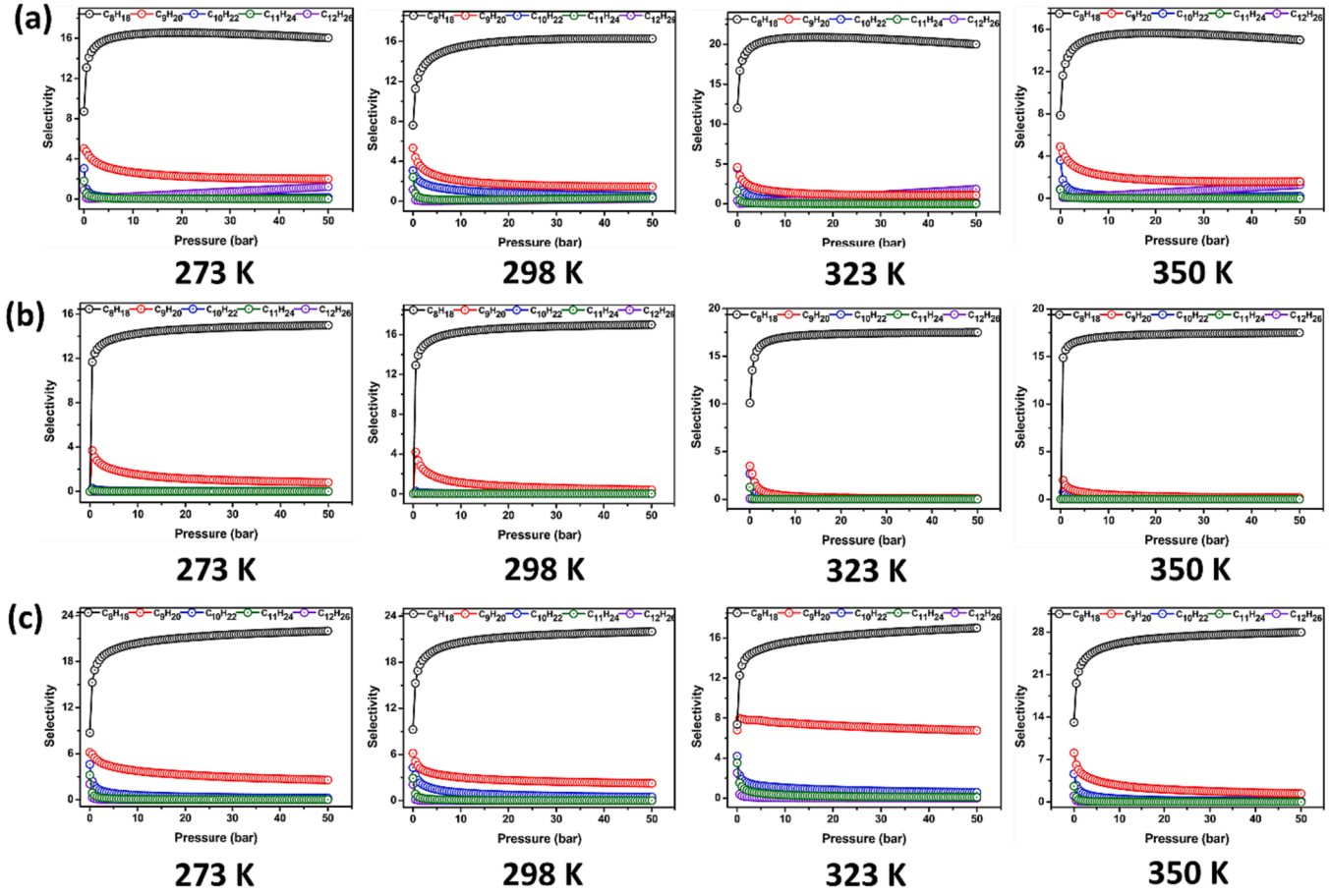

Fig. 7. The ideal adsorption solution theory employed selectivity of one component over the multicomponent mixture for the (a) Cu-PPX (b) Ag-PPX and (c) Au-PPX systems at various temperature and pressure.

HC mixtures. Similarly, at 323 K/50 bar, the selectivity of C9 in Au-PPX is 6.75 which is significantly higher and higher than Cu and Ag-PPX systems. It is inferred that the selective separation of C8 is more facile in all three forms of PPX and prominently high in Au-PPX, even at higher temperature and the selectivity of C9 and C12 is higher for Au-PPX and Cu-PPX respectively at 323 K/50 bar. So Cu-PPX and Au-PPX can be used as a good separator for separating the C8, C9, and C12 from the mixture components in the petrochemical industry.

Conclusions

The features of coinage metal-based PPX leading the host–guest complexation by entrapping linear chain HCs of C8–C12 has been investigated using DFT study. The result illustrates the formation of HC@Cu-PPX is more facile followed by Au-PPX and Ag-PPX. The binding energy portrays facile inclusion of the guest within the cavity of PPX host via dispersion van der Waals type dispersion contribution. The presence of –CH···N hydrogen bonding between the –CH portal of HCs and -N atom of pyrazole/imidazole is reveals an electrostatic interaction there exist in the complex. The magnitude of charge transfer from guest to host is higher in Cu-PPX system followed by Ag and Au-PPX and the electronic loss from the metal after complexation is higher for Au-PPX (0.022 e^-) followed by Ag (0.014 e^-) and Cu-PPX (0.007 e^-). The adsorption of HC within the PPX is ca. 59–62% ΔE_{disp} in nature and moderate ΔE_{elct} (ca. 22–24%) and ΔE_{orb} (15–16%) contribution. The maximum uptake of HC using PPX has obtained from GCMC simulation attributes C8 uptake is higher among all HCs. At ambient condition, the uptake is 18.01, 17.50 and 25.31 cm^3STP/g in Cu, Ag and Au-PPX respectively. The IAST analysis credits the selectivity of C8 is higher at the ambient condition as well as in high temperature and pressure system. It is observed that the C9 and C12 achieve good selectivity in Au and Cu-PPX system respectively upon increasing the temperature from 298 to 323 K. Thus it is noteworthy to mention that the Cu-PPX and Au-PPX are the ideal host to absorb the C8–C12 hydrocarbon and can be potentially used as a separator in the petrochemical industry.

CRediT authorship contribution statement

Biswajit Mohanty: Conceptualization, Methodology, Investigation, Visualization, Formal analysis, Project administration, Validation, Writing – original draft, Writing – review & editing. **Gopal Avashthi:** Resources, Supervision, Project administration, Writing – review & editing.

Declaration of Competing Interest

The authors declare that they have no known competing financial interests or personal relationships that could have appeared to influence the work reported in this paper.

Data availability

No data was used for the research described in the article.

Acknowledgments

The author thanks the C-DAC, Pune for the computational facility.

Appendix A. Supplementary data

Supplementary data to this article can be found online at https://doi.org/10.1016/j.rinp.2023.107016.

References

[1] Wu Y, Weckhuysen BM. Separation and purification of hydrocarbons with porous materials. Angew Chem Int Ed 2021;60:18930–49.
[2] Zeng Z, Wang W, Xiong X, Zhu N, Xiong Y, Wei Z, et al. Flexible microporous copper (II) metal-organic framework toward the storage and separation of C1–C3 hydrocarbons in natural gas. Inorg Chem 2021;60:8456–60.
[3] Xu S, Liu R-S, Zhang M-Y, Lu A-H. Designed synthesis of porous carbons for the separation of light hydrocarbons. Chin J Chem Eng 2022;42:130–50.
[4] Sun Y, Gao M-Y, Sun Y, Lu D-F, Wang F, Zhang J. Two isostructural titanium metal-organic frameworks for light hydrocarbon separation. Inorg Chem 2021;60:13955–9.
[5] M.A.B. Pauzan, M.A. Rahman, M.H.D. Othman, Hydrocarbon separation and removal using membranes, in: Membr. Technol. Enhanc. Environ. Prot. Sustain. Ind. Growth, Springer, 2021: pp. 73–90.
[6] Gao M-Y, Song B-Q, Sensharma D, Zaworotko MJ. Crystal engineering of porous coordination networks for C3 hydrocarbon separation. SmartMat 2021;2:38–55.
[7] Yang L, Qian S, Wang X, Cui X, Chen B, Xing H. Energy-efficient separation alternatives: metal–organic frameworks and membranes for hydrocarbon separation. Chem Soc Rev 2020;49:5359–406.
[8] Ababneh H, Al-Muhtaseb SA. A review on the solid–liquid–vapor phase equilibria of acid gases in methane. Greenh Gases Sci Technol 2022;12:566–79.
[9] Zhou S, Hwang BC, Lakey PS, Zuend A, Abbatt JP, Shiraiwa M. Multiphase reactivity of polycyclic aromatic hydrocarbons is driven by phase separation and diffusion limitations. Proc Natl Acad Sci 2019;116:11658–63.
[10] Li Y, Wang H, Cai Z, Zhang J, Fu J. Molecular analyses of petroleum hydrocarbon change and transformation during petroleum weathering by multiple techniques. ACS Omega 2021;6:23222–32.
[11] Bonneau M, Lavenn C, Ginet P, Otake K, Kitagawa S. Upscale synthesis of a binary pillared layered MOF for hydrocarbon gas storage and separation. Green Chem 2020;22:718–24.
[12] Herm ZR, Bloch ED, Long JR. Hydrocarbon separations in metal–organic frameworks. Chem Mater 2014;26:323–38.
[13] Peralta D, Chaplais G, Simon-Masseron A, Barthelet K, Chizallet C, Quoineaud A-A, et al. Comparison of the behavior of metal–organic frameworks and zeolites for hydrocarbon separations. J Am Chem Soc 2012;134:8115–26.
[14] Min JG, Kemp KC, Hong SB. Silver ZK-5 zeolites for selective ethylene/ethane separation. Sep Purif Technol 2020;250:117146.
[15] Yang Y, Burke N, Ali S, Huang S, Lim S, Zhu Y. Experimental studies of hydrocarbon separation on zeolites, activated carbons and MOFs for applications in natural gas processing. RSC Adv 2017;7:12629–38.
[16] Ma X, Chen R, Zhou K, Wu Q, Li H, Zeng Z, et al. Activated porous carbon with an ultrahigh surface area derived from waste biomass for acetone adsorption, CO2 capture, and light hydrocarbon separation. ACS Sustain Chem Eng 2020;8:11721–8.
[17] Orenha RP, Caramori GF, Parreira RLT, Munoz-Castro A. The use of molecular electronic structure methods to investigate mechanically interlocked molecules. PCCP 2023;25:19409–21.
[18] Quainoo T, Lavan SN, Liu Z-F. Van der Waals density functional study of hydrocarbon adsorption and separation in metal–organic frameworks without open metal sites. J Mater Res 2021;1–12.
[19] Li H, Wang K, Wu M, Hong M. A cage-based porous metal-organic framework for efficient C2H2 storage and separation. Chem Res Chin Univ 2021;1–5.
[20] Lu C, Bai H, Wu B, Su F, Hwang JF. Comparative study of CO2 capture by carbon nanotubes, activated carbons, and zeolites. Energy Fuels 2008;22:3050–6.
[21] Slawek A, Roztocki K, Majda D, Jaskaniec S, Vlugt TJ, Makowski W. Adsorption of n-alkanes in ZIF-8: Influence of crystal size and framework dynamics. Microporous Mesoporous Mater 2021;312:110730.
[22] Huang H, Zhang W, Liu D, Liu B, Chen G, Zhong C. Effect of temperature on gas adsorption and separation in ZIF-8: A combined experimental and molecular simulation study. Chem Eng Sci 2011;66:6297–305.
[23] Audu CO, Chen D, Kung C-W, Snurr RQ, Nguyen ST, Farha OK, et al. Transport diffusion of linear alkanes (C5–C16) through thin films of ZIF-8 as assessed by quartz crystal microgravimetry. Langmuir 2021;37:9405–14.
[24] Bhadra BN, Jhung SH. Selective adsorption of n-alkanes from n-octane on metal-organic frameworks: length selectivity. ACS Appl Mater Interfaces 2016;8:6770–7.
[25] Trung TK, Trens P, Tanchoux N, Bourrelly S, Llewellyn PL, Loera-Serna S, et al. Hydrocarbon adsorption in the flexible metal organic frameworks MIL-53 (Al, Cr). J Am Chem Soc 2008;130:16926–32.
[26] Oschatz M, Borchardt L, Rico-Francés S, Rodríguez-Reinoso F, Kaskel S, Silvestre-Albero J. Textural characterization of micro-and mesoporous carbons using combined gas adsorption and n-nonane preadsorption. Langmuir 2013;29:8133–9.
[27] Zhang J, Lu S, Li J, Zhang P, Xue H, Zhao X, et al. Adsorption properties of hydrocarbons (n-decane, methyl cyclohexane and toluene) on clay minerals: an experimental study. Energies 2017;10:1586.
[28] Autie-Pérez M, Infantes-Molina A, Cecilia JA, Labadie-Suárez JM, Rodríguez-Castellón E. Separation of light liquid paraffin C5–C9 with Cuban volcanic glass previously used in copper elimination from water solutions. Appl Sci 2018;8:295.
[29] Strange N, Larese JZ. High-resolution volumetric adsorption and molecular dynamics of the n-alkanes on the surface of hexagonal boron nitride. J Phys Chem C 2018;122:21308–21.
[30] Daems I, Baron GV, Punnathanam S, Snurr RQ, Denayer JF. Molecular cage nestling in the liquid-phase adsorption of n-alkanes in 5A zeolite. J Phys Chem C 2007;111:2191–7.

[31] Denayer JF, Devriese LI, Couck S, Martens J, Singh R, Webley PA, et al. Cage and window effects in the adsorption of n-alkanes on chabazite and SAPO-34. J Phys Chem C 2008;112:16593–9.
[32] G.V. Baron, S. Coeck, J.A. Martens, R. Singh, P.A. Webley, J.F. Denayer, Discontinuities in the low coverage adsorption of C1-C14 linear alkanes on NA-CHA and SAPO-34, in: Finds Results Swed. Cyprus Exped Gend Perspect Medelhavsmus, 2008.
[33] Liang Z, Marshall M, Chaffee AL. CO2 adsorption-based separation by metal organic framework (Cu-BTC) versus zeolite (13X). Energy Fuels 2009;23:2785–9.
[34] Dusselier M, Davis ME. Small-pore zeolites: synthesis and catalysis. Chem Rev 2018;118:5265–329.
[35] Altmann PJ, Pöthig A. Pillarplexes: A metal–organic class of supramolecular hosts. J Am Chem Soc 2016;138:13171–4.
[36] Chaudhary A, Mohammad A, Mobin SM. Recent advances in single-crystal-to-single-crystal transformation at the discrete molecular level. Cryst Growth Des 2017;17:2893–910.
[37] Rojas-Poblete M, Rodríguez-Kessler PL, Maturana RG, Muñoz-Castro A. Coinage-metal pillarplexes hosts. Insights into host–guest interaction nature and luminescence quenching effects. PCCP 2021;23:15917–24.
[38] Ponce-Vargas M, Munoz-Castro A. A study on the versatility of metallacycles in host–guest chemistry: interactions in halide-centered hexanuclear copper (ii) pyrazolate complexes. PCCP 2014;16:13103–11.
[39] Rojas-Poblete M, Rodríguez-Kessler PL, Guajardo-Maturana R, Ulloa CO, Muñoz-Castro A. Nature and role of formal charge of the ion inclusion in hexanuclear Platinum (II) Host-Guest Species. Insights from relativistic DFT calculations. Inorg Chim Acta 2023;546:121298.
[40] Parr RG. Density functional theory. Annu Rev Phys Chem 1983;34:631–56.
[41] Glendening ED, Landis CR, Weinhold F. Natural bond orbital methods. Wiley Interdiscip Rev: Comput Mol Sci 2012;2:1–42.
[42] Johnson ER, Keinan S, Mori-Sánchez P, Contreras-García J, Cohen AJ, Yang W. Revealing noncovalent interactions. J Am Chem Soc 2010;132:6498–506.
[43] Zhao L, von Hopffgarten M, Andrada DM, Frenking G. Energy decomposition analysis. Wiley Interdiscip Rev: Comput Mol Sci 2018;8:e1345.
[44] Puibasset J, Pellenq R-J-M. Grand canonical Monte Carlo simulation study of water adsorption in silicalite at 300 K. J Phys Chem B 2008;112:6390–7.
[45] Sircar S, Mohr R, Ristic C, Rao MB. Isosteric heat of adsorption: theory and experiment. J Phys Chem B 1999;103:6539–46.
[46] Hand DW, Loper S, Ari M, Crittenden JC. Prediction of multicomponent adsorption equilibria using ideal adsorbed solution theory. Environ Sci Tech 1985;19:1037–43.
[47] K. Burke, J.P. Perdew, Y. Wang, Derivation of a generalized gradient approximation: The PW91 density functional, in: Electron. Density Funct. Theory, Springer, 1998: pp. 81–111.
[48] Chiodo S, Russo N, Sicilia E. LANL2DZ basis sets recontracted in the framework of density functional theory. J Chem Phys 2006;125:104107.
[49] Legge FS, Nyberg GL, Peel JB. DFT calculations for Cu-, Ag-, and Au-containing molecules. Chem A Eur J 2001;105:7905–16.
[50] Ehrlich S, Moellmann J, Reckien W, Bredow T, Grimme S. System-dependent dispersion coefficients for the DFT-D3 treatment of adsorption processes on ionic surfaces. ChemPhysChem 2011;12:3414–20.
[51] Boys SF, Bernardi F. The calculation of small molecular interactions by the differences of separate total energies. Some procedures with reduced errors. Mol Phys 1970;19:553–66.
[52] M.J. Frisch, G.W. Trucks, H.B. Schlegel, G.E. Scuseria, M.A. Robb, J.R. Cheeseman, G. Scalmani, V. Barone, B. Mennucci, G.A. Petersson, Gaussian 09, Revision D. 01, Gaussian, Inc., Wallingford CT, See Also URL Httpwww Gaussian Com. (2009).
[53] E.D. Glendening, A.E. Reed, J.E. Carpenter, 3.1. (b) Weinhold, P, J Am Chem Soc 102 (1980) 7211.
[54] Bader RF, Essén H. The characterization of atomic interactions. J Chem Phys 1984;80:1943–60.
[55] Bader RF. A bond path: a universal indicator of bonded interactions. Chem A Eur J 1998;102:7314–23.
[56] Lu T, Chen F. Multiwfn: a multifunctional wavefunction analyzer. J Comput Chem 2012;33:580–92.
[57] Civalleri B, Zicovich-Wilson CM, Valenzano L, Ugliengo P. B3LYP augmented with an empirical dispersion term (B3LYP-D*) as applied to molecular crystals. CrstEngComm 2008;10:405–10.
[58] Wolff SK. Analytical second derivatives in the Amsterdam density functional package. Int J Quantum Chem 2005;104:645–59.
[59] Van Lenthe JH, Faas S, Snijders JG. Gradients in the ab initio scalar zeroth-order regular approximation (ZORA) approach. Chem Phys Lett 2000;328:107–12.
[60] Phipps MJ, Fox T, Tautermann CS, Skylaris C-K. Energy decomposition analysis approaches and their evaluation on prototypical protein–drug interaction patterns. Chem Soc Rev 2015;44:3177–211.
[61] Rappé AK, Casewit CJ, Colwell KS, Goddard III WA, Skiff WM. UFF, a full periodic table force field for molecular mechanics and molecular dynamics simulations. J Am Chem Soc 1992;114:10024–35.
[62] Zhang T, Zhang Y, Katterbauer K, Al Shehri A, Sun S, Hoteit I. Phase equilibrium in the hydrogen energy chain. Fuel 2022;328:125324.
[63] Myers AL, Prausnitz JM. Thermodynamics of mixed-gas adsorption. AIChE J 1965;11:121–7.
[64] Khalfaoui M, Knani S, Hachicha MA, Lamine AB. New theoretical expressions for the five adsorption type isotherms classified by BET based on statistical physics treatment. J Colloid Interface Sci 2003;263:350–6.
[65] Zheng J, Lu Z, Wu K, Ning G-H, Li D. Coinage-metal-based cyclic trinuclear complexes with metal–metal interactions: theories to experiments and structures to functions. Chem Rev 2020;120:9675–742.